

LAP1 regulates nuclear plasticity to enable constrained migration

Yaiza Jung-Garcia^{1,2,3,4}, Oscar Maiques^{2,4}, Irene Rodriguez-Hernandez^{2,4}, Bruce Fanshawe⁴, Marie-Charlotte Domart⁵, Matthew J Renshaw⁶, Rosa M Marti⁹, Xavier Matias-Guiu¹⁰, Lucy M Collinson⁵, Victoria Sanz-Moreno^{2,4*} & Jeremy G Carlton^{1,3*}

¹ Organelle Dynamics Laboratory, The Francis Crick Institute, 1 Midland Rd, London NW1 1AT, United Kingdom. ² Barts Cancer Institute, Queen Mary University of London, John Vane Science Building, Charterhouse Square, London EC1M 6BQ, United Kingdom. ³ Division of Cancer Studies, School of Cancer and Pharmaceutical Sciences, King's College London, London, SE1 1UL, United Kingdom. ⁴ Randall Division of Cell and Molecular Biophysics, King's College London, London SE1 1UL, United Kingdom. ⁵ Electron Microscopy Science Technology Platform, The Francis Crick Institute, 1 Midland Road, London NW1 1AT, UK. ⁶ Advanced Light Microscopy Science Technology Platform, The Francis Crick Institute, 1 Midland Road, London NW1 1AT, UK. ⁷ Department of Dermatology, Hospital Universitari Arnau de Vilanova, University of Lleida, IRB Lleida, CIBERONC, 25198 Lleida, Spain. ⁸ Department of Pathology and Molecular Genetics, Hospital Universitari Arnau de Vilanova, University of Lleida, IRB Lleida, CIBERONC, 25198 Lleida, Spain.

* Equal contribution, co-corresponding authors

KEYWORDS: Nuclear envelope, bleb, migration, actomyosin contractility

CORRESPONDANCE: jeremy.carlton@kcl.ac.uk, v.sanz-moreno@qmul.ac.uk

ABSTRACT

Metastatic spread involves the dissemination of cancer cells from a primary tumour and their colonisation of distal sites. During this process, cancer cells must negotiate multiple physical constraints imposed by the microenvironment and tissue structure, and the biophysical properties of the nucleus place a physical challenge on this form of migration. By analysing nuclear genes upregulated during the acquisition of metastatic potential, we discovered increased expression of the inner nuclear membrane protein LAP1 in metastatic cell lines and at the leading edge of human primary tumours and in metastatic lesions. Human cells express two LAP1 isoforms (LAP1B and LAP1C), which differ in their amino terminus. We found that the longer isoform, LAP1B, binds more strongly to nuclear lamins and enhances nuclear mechanocoupling, whilst the shorter isoform, LAP1C, favours nuclear envelope blebbing and permits migration through physical constraints. Thus, we propose that LAP1B and LAP1C act together to support a permissive nucleus which overcomes the physical constraints that cancer cells face during metastatic spread.

INTRODUCTION

Metastatic spread accounts for the majority of cancer-related deaths^{1, 2} and there is an urgent need to understand how metastatic potential is acquired. Metastatic melanoma is the leading cause of death for skin cancers^{3, 4}. Melanoma cells can switch between different collective and individual migratory modes, can proteolytically degrade the extracellular matrix and can reprogramme cells in the tumour microenvironment to favour cancer cell survival, migration and invasion⁵⁻¹¹. Physical constraints, for example traversing tissue constrictions or the vascular endothelium, are a major barrier to metastatic spread^{12, 13} and cells must negotiate multiple constraints before colonising new sites. While the cytoplasm can accommodate large deformations, the biophysical properties of the nucleus make translocation of this organelle the rate-limiting step during constrained migration¹³. Nuclear mechanoproperties are regulated through protein-protein interactions between nuclear envelope (NE) proteins, the nuclear lamina and the cytoskeleton¹⁴⁻²⁰. Deficiencies in lamins can render NE membranes prone to rupture under mechanical stress, leaving the genomic DNA exposed to damaging agents in the cytoplasm and prone to persistent damage due to the mis-localisation of repair factors²¹⁻²⁵. NE ruptures occur typically at NE blebs, where local remodelling of the lamina can allow NE and chromatin herniations to protrude into the cytoplasm²⁶. NE bleb formation is enhanced by actomyosin contractility, whereas nuclear stiffness enhances mechanocoupling at this organelle, facilitating the transmission of forces to the nucleus^{26, 27}. A deformable nucleus can adopt a variety of morphologies for negotiation of constraints and as such, the biophysical properties of nuclei in cells undergoing constrained migration must achieve a balance of stiffness and suppleness to allow this mode of migration. Whereas plasma membrane blebs can facilitate bleb-based migration^{11, 28-30}, it is not yet known whether NE blebs contribute to cellular migratory programmes. Here, we challenged melanoma cells derived from primary tumours, and those derived from isogenic metastatic lesions to multiple migratory constraints to identify proteins that enable cells to negotiate these challenges. Using a combination of transcriptomics, biochemistry, microscopy and live-cell imaging we discovered that the inner nuclear membrane (INM) protein lamin-associated polypeptide 1 (LAP1) enhances the ability of metastatic cells to undergo repeated constrained migration and tissue invasion.

RESULTS

Metastatic melanoma cells can better negotiate repetitive constrained migration challenges than primary melanoma cells

Using a pair of isogenic melanoma cell lines from the same patient (WM983A, derived from the primary tumour; WM983B, derived from a metastatic lesion) stably expressing a nucleus-localised GFP (GFP-NLS), we designed a multi-round transwell assay (Fig.1a) to understand differential abilities of these cancer cells to negotiate multiple constraints during migration and form NE blebs. Using transwells with a range of pore sizes smaller than the average nuclear diameter, we found that during the first round of migration, whilst decreasing pore size impaired migration, metastatic WM983B cells were more effective at negotiating constraints than WM983A cells (Fig.1b and Supplementary Fig.1a). Pore transit of WM983B was accompanied by enhanced NE blebbing (Fig.1c and Supplementary Fig.1b, c). On a second round of migration using sequentially 8- μ m and 5- μ m transwells, we found that while WM983B cells could negotiate this second challenge with a similar efficiency to the first challenge, WM983A cells were severely compromised by this second challenge (Fig.1d, e and Supplementary Fig.1d). In addition, pore transit of WM983B noticeably enhanced NE blebbing (Fig.1f and Supplementary Fig.1e, f) suggesting that NE blebbing either promotes the migratory ability of metastatic melanoma cells, or that negotiating the constraint produces NE blebs.

We confirmed that WM983A and WM983B retain this migratory behaviour after a third round of constrained migration using sequentially 8- μ m, 8- μ m and 5- μ m pores (Supplementary Fig.1g, h). The percentage of translocated nuclei exhibiting NE blebs after this third transit was again enhanced relative to the cells that did not translocate, but was not enriched, suggesting that repeated constrictions are not selecting for a population of cells with elevated NE blebs (Supplementary Fig.1i, j). We confirmed that both cell lines have a similar number of viable cells after migration (Supplementary Fig.2a, b). We also confirmed that neither the morphological features of apoptosis nor active Caspase 3 were present in either of the melanoma cell lines, before or after a second-round of migration (Supplementary Fig.2b, c), suggesting that passage through repeated constraints does not activate a cell death programme.

WM983B display enhanced ROCK-driven Myosin II (MLC2) activity than WM983A^{8, 9, 31} (Supplementary Fig.2d). We reasoned that higher MLC2 activity hence higher actomyosin contractility could contribute to both the generation of NE blebs and the enhanced migration of WM983B over WM983A. To test this hypothesis, we treated cells with the ROCK inhibitor (ROCKi) GSK269962A and challenged them sequentially to migration through 8- μ m and 5- μ m transwell pores. We confirmed that MLC2 activity was reduced after ROCK inhibition (Supplementary Fig.2d, e) and found that ROCK inhibition did not reduce nuclear translocation but did reduce NE blebbing of WM983B during the first round of migration (Fig.1g, h). However, ROCK inhibition markedly impaired nuclear translocation during the second round (Fig.1i), suggesting that passage through the first constraint activates a ROCK-dependent migration programme for subsequent passages. Notably, we also observed a considerable reduction in the proportion of WM983B with NE blebs after pore transit on the second round in cells treated with ROCKi (Fig.1j) suggesting that actomyosin contractility contributes to the generation of these blebs. We concluded that ROCK-driven actomyosin contractility is required for NE bleb generation and nuclear translocation of melanoma cells through repeated constraints.

The nuclear envelope of metastatic melanoma cells is highly dynamic

We next hypothesised that metastatic melanoma cells that had already negotiated multiple constraints *in-vivo* may have retained a nuclear mechanical memory. We examined the nucleus of unconfined melanoma cells with variable metastatic potential to determine whether there were underlying differences in the degree of NE blebbing. Lamin A/C immunofluorescence revealed that 30% of WM983B display NE blebs compared to only 5% of WM983A (Fig.2a). We defined four main NE bleb categories according to bleb shape (Fig.2b, c) and discovered that there were more NE blebs per nucleus and higher bleb phenotypical variability in WM983B compared to WM983A (Fig.2c) re-enforcing the association of NE pleiomorphisms with melanoma aggressiveness. Furthermore, we scrutinised the NE of melanocytes and found NE blebs only in 1% of cells (Supplementary Fig.3a, b) suggesting that the degree of nuclear blebbing correlates with the progression of the disease.

To assess NE blebbing in a more physiological setting, we examined melanoma cells seeded in collagen I matrices. We confirmed that WM983B in collagen I were more amoeboid and harboured higher MLC2 phosphorylation levels than WM983A (Supplementary Fig.3c-e, i). These cells had a more irregular nucleus, with 20% of WM983B in collagen displaying NE blebs compared to 10% of WM983A and a higher karyoplasmic ratio (Supplementary Fig.4j, k, l, p). We obtained similar results with another melanoma cell line pair (highly metastatic and highly amoeboid A375M2 cells and less metastatic and less amoeboid A375P cells^{9, 31, 32} (Supplementary Fig.3f-i, m-p)). Therefore, we suggest that the more metastatic and amoeboid the melanoma cells are, the more likely they are to display NE blebs.

NE blebs form at regions of the NE with compromised structural integrity^{21-24, 26}. We investigated if NE blebs in melanoma cells were associated with local changes in nuclear lamins. We found that about 90% of NE blebs present a weak or absent B-type lamin staining but maintain persistent lamin A/C staining (Fig.2d, e). In addition, chromatin extruded in NE blebs and was frequently positive for markers of double-strand DNA breaks (Supplementary Fig.4a, b), which suggests they are spots for local DNA damage generation. Nevertheless, overall levels of DNA damage were not increased (Supplementary Fig.4c).

We examined the dynamics of NE bleb formation, rupture and repair using unconfined melanoma cells stably expressing GFP-NLS. We found that NE blebs could either be intact or ruptured and this was further assessed using correlative light and electron microscopy (CLEM) demonstrating clear rupture of the NE at the bleb with concomitant leakage of the GFP-NLS signal (Fig.2f and Supplementary Movies 1a, 1b, 2a, 2b). We found that ruptured NE blebs were more frequent than intact blebs and that WM983B exhibit more ruptured NE blebs than WM983A (Fig.2g). We wondered whether cytoskeletal forces imposed on the nucleus were responsible for inducing NE blebbing and rupture. Indeed, both NE blebbing and ruptures were abrogated by ROCK inhibition in both WM983A and WM983B (Fig.2h). To preserve cellular viability during interphase NE ruptures, cells reseal their NE via ESCRT-III-dependent repair^{24, 26}. We found that NE ruptures in melanoma cells are transient and that both WM983A and WM983B display similar NE repair kinetics with an average repair time of 10 minutes (Fig.2i). Consistent with a higher background level

of NE instability in WM983B, the rupture-repair rate for these cells was higher than WM983A, with up to one event per hour (Fig.2j, Supplementary Fig.4d, e and Supplementary Movies 3, 4). These results suggest that NE ruptures occur at sites depleted of B-type lamins, that they are more frequent in metastatic cells and that an efficient NE repair programme acts to preserve cellular viability.

Nuclear transcriptomics reveals *TOR1AIP1* upregulation in metastatic cells

As the degree of NE blebbing and migratory ability correlates with disease progression (Fig.1 and Supplementary Fig.1, 3), we interrogated a previously published transcriptomic microarray of highly metastatic and highly amoeboid A375M2 cells compared to less metastatic and less amoeboid A375P cells^{6-8, 31}. We used Gene Set Enrichment Analysis (GSEA) to compare the transcriptomes of A375M2 and A375P cells focussing on genes encoding nuclear proteins (Fig.3a). This analysis showed that 63% of the gene sets containing genes encoding nuclear proteins were upregulated in A375M2 cells, while A375P cells showed only 1% upregulation of these gene sets (Fig.3b). Strikingly, about one third of upregulated gene sets in A375M2 were related to the nuclear membrane and organelle organisation (Fig.3b and Supplementary Tables 1-12). Leading-Edge Analysis³³ allowed us to identify a cluster of concurrently upregulated genes across NE gene sets (Fig.3c). Individual gene upregulation and statistical significance were evaluated and a final list of 7 candidate genes showing statistically significant upregulation was compiled (Fig.3e). For many of these genes, transcriptomic analysis of A375M2 compared to A375M2 treated with several contractility inhibitors (ROCK inhibitors H1152 or Y27632 or myosin II inhibitor blebbistatin) yielded similar results (Fig.3d, e). Candidate gene upregulation in A375M2 compared to A375P was confirmed by qPCR. Whilst all of the genes were upregulated in A375M2, *OSBPL8*, *SUMO1* and *TOR1AIP1* achieved statistical significance (Fig.3f). Exploring this in an orthogonal system, we confirmed statistically significant upregulation of *TOR1AIP1* by qPCR in WM983B compared to WM983A (Fig.3g).

To assess how the expression of our candidate genes changes in melanoma progression, gene expression was analysed in two datasets (Philadelphia and Mannheim³⁴) containing collections of melanoma cell lines compared to

melanocytes. In both cases, upregulation of all our candidate genes was consistent across melanoma cell lines compared to melanocytes (Fig.3h). Furthermore, using publicly available patient datasets (Kabbarah ³⁵, Riker ³⁶ and Xu ³⁷), we found that *TOR1AIP1* mRNA levels were consistently upregulated in human samples derived from metastatic melanoma lesions compared to primary melanoma (Fig.3i). These data suggest that expression of *TOR1AIP1* is upregulated in metastatic melanoma.

LAP1 is overexpressed in melanoma metastasis

We next assessed the expression of the protein encoded by *TOR1AIP1*, LAP1, *in-vivo* by staining mouse xenograft derived from WM983A or WM983B cells with antisera raised against LAP1. High-resolution immunohistochemistry coupled to digital pathology revealed that LAP1 localised to the NE. We observed that LAP1 expression was higher at the invasive fronts (IF) compared to the tumour bodies (TB) of WM983A and WM983B xenograft tumours (Fig.4a, b). We scored LAP1 intensity from 0 (very low) to 3 (very high) in individual tumour cell nuclei and observed that tumour cells showing the highest levels of LAP1 had a higher karyoplasmic ratio and represented a higher proportion in WM983B xenografts compared to WM983A xenografts (Fig.4c and Supplementary Fig.5a). We confirmed these observations in A375P and A375M2 xenograft tumours and found that they retained the same LAP1 staining pattern (Fig.4d-f and Supplementary Fig.5b).

We next assessed LAP1 expression in human tissue from normal skin and melanoma. In agreement with our *in-vitro* data, we found that LAP1 expression was very low in melanocytes compared to keratinocytes (Supplementary Fig.5c, d). We next used tissue microarrays from two human melanoma patient cohorts (cohort A including 19 primary tumours and 14 metastases and cohort B with a total of 29 matched primary tumours and metastases ³¹) (Supplementary Tables 13, 14). We found increased LAP1 expression in IFs compared to the TBs of primary tumours and in metastatic lesions compared to primary tumours (Fig.4g-l). Importantly, we observed that tumour cells showing very high LAP1 had a higher karyoplasmic ratio and represented a higher proportion in TBs and IFs of human melanoma metastases compared to the TBs and IFs of primary melanoma tumours (Fig.4i, l and Supplementary Fig.5e, f).

LAP1 is required for repeated constrained migration

Human cells express two isoforms of LAP1 that differ in the length of their amino terminus (NT); a long isoform, LAP1B, and a shorter isoform, LAP1C, generated by use of an alternative translation initiation at codon 122³⁸ (Fig.5a). We quantified the expression of LAP1B and LAP1C in melanocytes, primary melanoma cells and metastatic melanoma cells. Consistent with our transcriptomic analyses, we found that both LAP1 isoforms were upregulated in metastatic cells (Fig.5b, c).

We took a loss of function approach to understand whether LAP1 contributes to NE blebbing and the enhanced migration of WM983B cells. Whilst LAP1 isoforms were relatively resistant to siRNA depletion, by careful titration of the siRNA pool, we were able to reduce expression of LAP1 isoforms in WM983B to match levels observed in WM983A (Fig.5d and Supplementary Fig.6a). We performed multi-round transwell migration assays and discovered that reducing LAP1 expression levels in WM983B resulted in a reduction of 40% in second-round migration efficiency (Fig.5e) with no effect on cell viability (Supplementary Fig.6b). LAP1 depletion also suppressed NE blebbing associated with the second round of transwell migration in WM983B (Fig.5f). We confirmed these results using two independent LAP1 siRNAs (Supplementary Fig.S6c-e). We next performed 3D-invasion assays to assess the impact of LAP1 depletion on the ability of metastatic melanoma cells to invade through complex collagen I matrices. We found that reduced LAP1 expression levels decreased the ability of WM983B to invade into collagen (Fig.5h, i). Overall, these data suggest that as well as being required for NE-bleb generation, LAP1 has a role in supporting the ability of metastatic melanoma cells to negotiate constraints in the microenvironment.

LAP1B and LAP1C are differentially tethered to nuclear lamins

We next set out to understand if LAP1 isoforms play different roles based on the distinct length of their N-termini. We carried out a solubilisation assay, and in agreement with previous studies³⁸ found that LAP1C was released from the nucleus under mild extraction conditions, whereas LAP1B was only released when the nuclear lamina was solubilised (Supplementary Fig.7a). These data suggested that LAP1B might be involved in stronger protein-protein interactions with the nuclear lamina. Nuclear lamins are key nuclear mechanosensors¹⁸. The NT of LAP1

interacts with lamin A/C and lamin B1³⁹ and Luithle et al, have recently demonstrated the existence of two distinct lamin-binding regions in LAP1's NT: 1-72 (present in the unique region of LAP1B) and 184-337 (present in both LAP1B and LAP1C)⁴⁰. We hypothesised that the different length of the N-termini of LAP1 isoforms might encode differential lamin-binding properties.

Solubilising INM proteins for classical immunoprecipitation approaches, whilst retaining native interactions, is challenging. We instead employed a mitochondrial retargeting assay and expressed GFP-Lamin A/C or GFP-Lamin B1 and either LAP1B^{NT}, LAP1C^{NT} or the unique region of LAP1B's NT (LAP1B^{uNT}) fused to HA and the mitochondrial targeting sequence from Monoamine Oxygenase⁴¹ (HA-MTS). We looked for mitochondrial re-localisation of GFP-Lamins or relocalisation of HA-tagged mitochondria to the nucleus and NE as a readout of this interaction (Fig.6a). We found that mitochondria presenting HA-LAP1B^{NT} or HA-LAP1B^{uNT} on their surface could be strongly relocalised to the GFP-Lamin positive NE, whereas mitochondria expressing HA-LAP1C^{NT} were less able to be relocated (Fig.6b, c). Consistent with the presence of a chromatin-binding domain in LAP1B's NT⁴⁰, mitochondria presenting this region were strongly relocalised to the chromatin periphery. In all cases, expression of the HA-LAP1 N-termini on mitochondria induced their clustering, but mitochondria that did not relocalise to the NE were able to strongly recruit GFP-Lamin B1, but not GFP-Lamin A/C. We suggest that as well as containing a chromatin binding region⁴⁰, the unique NT of LAP1B encodes a dominant lamin-binding domain that displays preference for B-type lamins.

Using cells stably expressing C-terminal mRuby3-tagged versions of LAP1C or LAP1B (M122A) (Supplementary Fig.7b), we observed that LAP1B-mRuby3 like GFP-Lamin B1, was largely excluded from NE blebs, whereas LAP1C-mRuby3 and GFP-Lamin A/C were able to enter NE blebs (Supplementary Fig.7c, d). Using Fluorescence Recovery After Photobleaching (FRAP), we discovered that LAP1C-mRuby3 was more mobile than LAP1B-GFP both at the main NE and in NE blebs (Supplementary Fig.7e, f and Supplementary Movies 5a-c), in agreement with previous studies in other systems⁴⁰. We suggest that LAP1 isoforms are differentially mobile in the INM with LAP1B displaying stronger anchoring to chromatin and B-type lamins through its extended NT, whilst LAP1C presents less

strong tethers to the lamina and can move more freely in the INM to populate NE blebs.

LAP1C supports a nucleus permissive for blebbing and constrained migration

We next wondered if LAP1 isoforms made a differential contribution to constrained cell migration. In multi-round transwell migration assays, we observed that expression of LAP1C-mRuby3 in WM983A cells increased both migration efficiency and NE blebbing (Fig.7a, b). We used this gain-of-function system to explore requirements for individual LAP1-isoforms in modulating mechanical properties of the nucleus, permitting NE blebbing and supporting constrained migration. We found that the effect of LAP1C in supporting multi-round migration was concentration dependent (Supplementary Fig.8) suggesting that its presence provides a dominant advantage to this process. Interestingly, expression of LAP1B-mRuby3 in WM983A cells neither increased migration efficiency nor NE blebbing (Fig.7a, b). Expression of both isoforms of LAP1 from LAP1-mRuby3 in WM983A similarly enhanced migratory capacity and NE blebbing (Fig.7a, b). We concluded that LAP1C is the dominant isoform allowing NE blebbing and conferring an ability for metastatic melanoma cells to migrate through multiple constraints.

Finally, we generated versions of LAP1B lacking either the dominant lamin-binding domain (LAP1B^{Δ1-72}-mRuby3) or the chromatin-binding domain (LAP1B^{ΔC_{BR}}-mRuby3) (Fig.7c). Expression of LAP1B^{Δ1-72}-mRuby3 or LAP1B^{ΔC_{BR}}-mRuby3 in WM983A cells enhanced both NE blebbing and migration in multi-round transwell assays (Fig.7d-g), suggesting that an interplay between lamin and chromatin tethers restricts NE blebbing and the nuclear shape rearrangements required for constrained migration. We validated the contribution of a truncated NT in constrained migration using siRNA resistant versions of wild-type and mutant LAP1B-mRuby3. Here, stable expression of LAP1B^{Δ1-72}-mRuby3 or LAP1B^{ΔC_{BR}}-mRuby3, in a background of LAP1-depletion, allowed cells to generate NE blebs and perform multi-round constrained migration (Fig.7h, i).

Altogether, our data show how the distinct tethering of LAP1 isoforms to the lamina and chromatin enables metastatic melanoma cells to efficiently negotiate physical

challenges. Moreover, LAP1 isoforms differentially contribute to nuclear plasticity under constrained migration with LAP1B reinforcing lamina and chromatin tethers and LAP1C controlling nuclear deformability and licensing negotiation of physical constraints.

DISCUSSION

Mechanotransduction at the cell nucleus relies on the connections between the nucleoskeleton and the cytoskeleton^{15, 18}. Our work uncovers a role for ROCK-driven actomyosin contractility in fitting the nucleus of metastatic melanoma cells to negotiate multiple physical constraints during migration. We suggest that a plastic nucleus is a feature conferring an advantage to migrating cells under mechanical challenge.

Here, we describe that expression of *TOR1AIP1* and its encoded protein, the INM protein, LAP1, is upregulated in metastatic melanoma cells. Moreover, we observed that LAP1 is enriched at the IFs of xenograft melanoma tumours and patient metastatic lesions. Strikingly, we found that LAP1 isoforms play distinct functions. We highlight that the longer NT of LAP1B, and specifically residues 1-72, enable a strong interaction with nuclear lamins. Interestingly, alterations in the coupling between the nucleoskeleton and the cytoskeleton impact mechanotransduction²⁷, suggesting that LAP1B upregulation may facilitate the contractile response that allows NE blebbing. At the same time, the (re)establishment of LAP1B and nuclear lamins or chromatin tethers might counteract the effect of the mechanical loading and promote cell survival^{16, 26}. We found that LAP1C, encoding a protein with a shorter NT lacking both the dominant lamin-binding domain and an internal chromatin-binding domain, is more mobile within the NE. Consistent with a more limited tethering to the underlying nuclear lamina and chromatin, this isoform supports enhanced NE blebbing and provides an advantage for migration through repeated constraints. We should note that whilst we report enhanced NE blebbing being associated with repetitive constrained migration, it is not clear whether blebs arise as a consequence of forcing a permissive nucleus through a constraint, or whether the blebs themselves play an active role in negotiating this constraint. Whilst plasma membrane blebs were originally thought to occur as the passive

consequence of cortical contractility, we now know they play active roles in altering migratory programmes⁴². NE blebs form and burst due to intranuclear pressure^{26, 43}, which can also cause nuclear membranes to unfold in a cellular contractile response to overcome confinement^{27, 44}. The nucleus of tumour cells is known to soften whilst passing constraints⁴⁵⁻⁴⁷, which is also consistent with nuclear deformability supporting constraint negotiation. We speculate that a nucleus that is more mechanosensitive and has the ability to selectively reinforce or deform its membranes would confer an advantage to tumour cells negotiating external physical constraints.

In the light of our results, we propose that LAP1B and LAP1C sustain migration and invasion of metastatic melanoma cells through multiple constraints. Thus, we suggest that modulating LAP1 expression could be a route to prevent metastatic dissemination.

ACKNOWLEDGMENTS

J.C.G is a Wellcome Trust Senior Research Fellow (206346/Z/17/Z), VSM is a Cancer Research UK (CRUK) Senior fellow and VSM lab was supported by (CRUK) C33043/A24478; Barts Charity; Fundacion Alfonso Martin Escudero and Marie Sklodowska-Curie Action, grant agreement No 659022. Y.J.-G. received a Crick-KCL PhD studentship. We thank Eva Crosas-Molist and Jose L. Orgaz (Barts Cancer Institute, UK) for their supervision with cell biology experiments. This work was supported in part by the Francis Crick Institute which receives its core funding from Cancer Research UK (FC001002), the UK Medical Research Council (FC001002), and the Wellcome Trust (FC001002). For the purpose of Open Access, the author has applied a CC BY public copyright licence to any Author Accepted Manuscript version arising from this submission.

AUTHOR CONTRIBUTIONS

J.C.G. and V.S.-M. were principal investigators, designed the research, supervised experiments and wrote the paper; Y.J.-G. designed the research, performed the experiments, analysed the data, wrote the paper; O.M. assisted with the immunohistochemistry; I.R.-H. assisted with the transcriptomic analyses and qPCR; B.F. generated the mouse xenografts; M.C.D. and L.M.C. performed and supervised

the CLEM experiments; M.R. trained for and supervised the FRAP experiments; R.M.M. and X.M.G provided the human tissue.

COMPETING INTERESTS

The authors declare no competing interests.

MATERIALS AND METHODS

Cell culture. The human melanoma cells WM1361 and WM1366 were from Professor Richard Marais (Cancer Research UK Manchester Institute); the human melanoma cells WM793B, WM983A, WM983B and WM88 were purchased from the Wistar Collection at Coriell Cell Repository; the human melanoma cells A375P and A375M2 were from Dr. Richard Hynes (HHMI, MIT); the human primary melanocytes M206 and M443 isolated from foreskin were from Dr. Beatriz Jiménez (Universidad Autónoma de Madrid and Instituto de Investigaciones Biomédicas CSIC-UAM, Spain); HEK293T and CAL51 were from Dr. Jeremy Carlton (The Francis Crick Institute, UK). WM1361 and WM793B were cultured in Roswell Park Memorial Institute (RPMI, Gibco) medium supplemented with 10% of foetal bovine serum (FBS) and 1% (v/v) penicillin and streptomycin (PenStrep, Gibco); HEK293T, CAL51, WM1366, WM983A, WM983B, WM88, A375P and A375M2 were cultured in Dulbecco's modified Eagle's media (DMEM, Gibco) supplemented with 10% FBS and 1% (v/v) PenStrep; M206 and M443 were cultured in (MGM-4, Lonza) supplemented with 1 ml CaCl₂, 2 ml BPE, 1 ml rhFGF-B, 1 ml rh-Insulin, 0.5 ml Hydrocortisone, 0.5 ml PMA, 0.5 ml GA-1000, 0.5% FBS and 1% (v/v) PenStrep. Cells were grown at 37°C and 5% or 10% CO₂. Cells were kept in culture to a maximum of three or four passages.

Plasmids. pTRIP-SFFV-EGFP-NLS and the coding sequences of mEmerald-Lamin A/C and mEmerald-Lamin B1 were from Addgene. pLVX-N-GFP was a kind gift from Prof. Michael Way (The Francis Crick Institute, UK) and was modified to express mEmerald-Lamin A/C or mEmerald-Lamin B1 by replacing GFP. The coding sequence for LAP1 was from Integrated DNA Technologies. LAP1C, point mutations in LAP1B (M122A, Δ 1-72m, Δ CBRm) and deletion of 1-72 residues (Δ 1-72) in LAP1B were generated using standard PCR. All PCR primers are in Supplementary Table 15. LAP1B carrying the deletion of the chromatin binding region (Δ CBR) was from Integrated DNA Technologies. LAP1, LAP1C and LAP1B mutants were cloned into pCMS28-EcoRI-NotI-XhoI-Linker-mRuby3. LAP1B (M122A) was also cloned into pNG72-EcoRI-NotI-XhoI-LAP-GFP. LAP1B^{NT}, LAP1B^{uNT} or LAP1C^{NT} were cloned into pCR3.1 with HA-MTS.

Transient transfection. CAL51 or WM983B cells were seeded at a density of 8×10^4 cells in 4-well or 24-well plates and transfected with 0.5 μ g of vector construct using optimem (Gibco), lipofectamine 3000 and P3000 (Invitrogen). Media was changed 6 hours post-transfection. At 48-hours post-transfection, CAL51 cells were fixed with 4% formaldehyde (FA) for 15 minutes at room temperature (RT).

Generation of stable cell lines. HEK293T cells were seeded at a density of 4×10^5 cells/ml in 6-well plates. For lentiviral production, cells were transfected with 1.5 μg of lentiviral vector, 0.5 μg of pVSVG and 2 μg of HIV-1 pCMVd8.91 using optimem, lipofectamine 3000 and P3000. For retroviral production, cells were transfected with 1.5 μg of retroviral vector, 0.5 μg of pHIT-VSVG and 2 μg of MLV-GagPol using optimem, lipofectamine 3000 and P3000. Media was changed 6 hours post-transfection. Viral supernatants were collected 48 hours post-transfection, spun down and filtered (0.2 μm). Melanoma cells seeded at a density of 2×10^5 in 6-well plates were infected with filtered supernatants. Antibiotic selection as required was started 48 hours post-infection. For assessing the concentration effect of LAP1C, cells were harvested in FACS buffer (PBS, 5mM EDTA, 2% FCS, 1mM HEPES) and sorted according to LAP1C-mRuby3 fluorescence intensity levels.

siRNA transfection. Melanoma cells were seeded at a density of 4×10^4 cells/ml in 24-well plates or 5×10^5 in 6-well plates and transfected one hour after seeding. Cells were transfected with 20 mM siGenome Smart Pool or On-Targetplus LAP1 siRNA oligonucleotides using optimem and lipofectamine RNAiMax (Invitrogen). All siRNA oligonucleotides were from Dharmacon and are listed in Supplementary Table 16. Non-targeting siRNA was used as a control. Multi-round transwell migration and invasion assays were carried out 48-hours post-transfection.

Transwell migration assays. Cells were starved in serum-free DMEM overnight and seeded at a density of 1.65×10^5 cells/ml per insert in 24-well plates or 2.335×10^6 cell/ml per insert in 6-well plates. DMEM 10% FBS was used as chemoattractant. Cells were allowed to migrate 16 hours in 24-well plates and 24 hours in 6-well plates. For multi-round transwell assays, cells were collected after one round from inserts in 6-well plates and seeded on inserts in 24-well plates. Cells were fixed with 4% FA for 15 minutes at RT. Transwell inserts were from Corning.

Inhibitor treatments. ROCKi GSK269962A (Axon MedChem) was used at 1 μM and Staurosporin (Cell Guidance Systems) was used at 1 μM . In transwell assays, the inhibitor was added to the chemoattractant.

Quantitative real-time PCR (qPCR). Melanoma cells were seeded at a density of 1×10^5 cells/ml in 12-well plates 24 hours prior to the experiment. RNA was extracted using Trizol (Life Technologies) following manufacturer's instructions. RNA was treated with DNA-free™ DNA Removal Kit (Life Technologies) and RNA purity was determined with a ND-1000 Nanodrop (Thermo Fisher Scientific). qPCRs were performed using 100 ng RNA, QuantiTect primer assays and Brilliant III SYBR Green QRT-PCR Kit (Agilent Technologies) in a ViiA 7 Real-Time PCR System (Thermo Fisher Scientific). GAPDH was used as loading control. The following qPCR primers from Qiagen were used: RANBP2 (QT00035378), TPR (QT00046242), OSBPL8 (QT00067102), SUMO1 (QT00014280), NUP50 (QT00081669), ZMPSTE24 (QT00025627), TOR1AIP1 (QT00070147).

Western blotting. Melanoma cells were seeded at a density of 6×10^5 cells/ml in 12-well plates and lysed on the next day with LDS buffer 1X (Life Technologies). Lysates were denatured at 95° C for 5 minutes, sonicated and spun down. SDS-page electrophoresis was run at 150 V for 50 minutes. Transfer to PVDF membranes was run at 200 mA fixed for 90 minutes. Membranes were blocked for one hour in 5%

BSA and incubated with primary antibody in 5% BSA overnight at 4° C in an orbital shaker. On the next day, membranes were incubated in secondary antibody in 5% BSA for 45 minutes at RT in an orbital shaker. Membranes were visualised using Odyssey Fc (LI-COR) and protein quantification was done with Odyssey Fc associated software. Primary antibodies were: LAP1 (1:1000; #21459-1-AP) from Proteintech; pThr18/Ser19-MLC2 (1:750, #3674) and MLC2 (1:750, #3672) from Cell Signalling Technology; GAPDH (1:10,000, #MAB374) from Merck. Secondary antibodies were: IRDye 680RD goat anti-rabbit IgG (1:10,000, v925-68071) and IRDye 800RD goat anti-mouse IgG (1:10,000, #925-32210) from LI-COR.

Cell culture on thick layers of collagen type I. Collagen I matrices were prepared using FibriCol (CellSystems) at 1.7 mg/ml. Collagen was left 4 hours to polymerise and melanoma cells were seeded on top at a density of 5×10^3 in 96-well plates. Medium was changed the next day to DMEM 1% FBS. After 24 hours, cells were fixed with 20% FA for 15 minutes at RT. For nuclear staining, cells were fixed with 2% FA for 30 minutes at RT.

3D invasion assays. Collagen I was prepared using FibriCol at 2.3 mg/ml. Melanoma cells were suspended in serum-free DMEM to a final concentration of 1.5×10^4 cells per 100 μ l of collagen. Cells were centrifuged at 1800 rpm and 4°C for 8 minutes, resuspended in collagen and seeded on glass bottom 96-well plates (Ibidi). The plates were centrifuged at 900 rpm for 5 minutes to get all the cells at the bottom. Collagen was left 4 hours to polymerise and DMEM 10% FBS was added to the top. Cells were allowed to invade for 24 hours. Cells were fixed with 20% FA overnight at 4°C.

Immunofluorescence staining. Cells in coverslips were fixed with 4% FA for 15 minutes at RT, permeabilised with 0.3% triton for 20 minutes, blocked with 4% bovine serum albumin (BSA) for 30 minutes and incubated sequentially with primary antibody in 4% BSA for two hours at RT and secondary antibody in 4% BSA for one hour at RT. DNA was stained with DAPI 1:1000 or Hoechst 1:5000 in PBS (Gibco). For DNA damage staining, cells were washed in PBS and incubated with CSK buffer (10 mM Pipes, pH 6.8, 100 mM NaCl, 300 mM sucrose, 3 mM MgCl₂, 10mM B-glycerol phosphate, 50mM NaF, 1mM EDTA, 1mM EGTA, 5mM Na₂VO₃, 0.5% Triton) for three minutes and again for 1 minute on ice pre-fixation. Cells were fixed with 4% FA for 20 minutes on ice, blocked with 10% goat serum for one hour at RT and incubated sequentially with primary antibody in 1% goat serum overnight at 4°C and with secondary antibody in 1% goat serum for one hour at RT. For nuclear staining in collagen I, cells were permeabilised with 0.5% triton for 30 minutes, blocked with 4% BSA overnight at 4°C, incubated with primary antibody in 4% BSA overnight at 4°C and with secondary antibody in 4% BSA for two hours at RT. Primary antibodies were: lamin A/C (1:200, #10298-1-AP) from Proteintech or (1:200; #mab3538) from Millipore; lamin B1 (1:200, # 12987-1-AP), lamin B2 (1:200, #10895-1-AP) and LAP1 (1:200; #21459-1-AP) from Proteintech; pSer19-MLC2 (1:200, #3671) from Cell Signalling; HA.11 (1:500, #901503) from BioLegend; Gamma-H2AX (1:600, #05-636) from Merck; 53BP1 (1:600, #NB100305) from Novus Biologicals. Secondary antibodies were Alexa Fluor 488 and Alexa Fluor 555 (1:1000) from Sigma or Invitrogen raised against the corresponding species. F-actin was stained using Alexa Fluor 546-phalloidin from Life Technologies and DNA with Hoechst 33342 from Invitrogen.

Confocal fluorescence microscopy and image analysis. Images were acquired with a Dragonfly 200 high speed confocal microscope (Andor). Imaging was carried out with 20X or 60X oil objectives. Z-stacks of 1-5 μm step-size distance were acquired from fixed cells in 2D, transwells and collagen I. Live cell imaging was done at 37°C and 5% CO_2 in a sealed chamber. Movies were taken at 2-minutes intervals for 1-15 hours. Image analysis was carried out using ImageJ. Fluorescence signal intensities were quantified from pixel intensity in single cells relative to the areas of interest.

Fluorescence recovery after photobleaching. Cells were seeded at a density of 8×10^4 in 4-well plates (Ibidi) 24 hours prior to the experiment. A LSM 880 Carl Zeiss microscope was used for imaging. Cells were kept at 37°C and 5% CO_2 in a sealed chamber. Cells were imaged with a 63 x 1.4 NA objective. First, 5 pre-bleached values were acquired and then squares of 1.3 X 1.3 ($1.69 \mu\text{m}^2$) at the main NE and at NE blebs were bleached with 50% 405 nm laser intensity. Fluorescence recovery was measured every second for 200 cycles. The FRAP data was curated subtracting background and normalised.

Correlative light and electron microscopy. Correlative light and electron microscopy. Melanoma cells were seeded at a density of 2×10^5 in 35 mm gridded glass-bottom dishes (MatTek) 24 hours prior to the experiment. Live cells were imaged until nuclear envelope rupture was spotted, at which point cells were fixed adding 8 % (v/v) formaldehyde (Taab Laboratory Equipment Ltd, Aldermaston, UK) in 0.2 M phosphate buffer (PB) pH 7.4 to the cell culture medium (1:1) for 15 minutes. Cells were mapped using brightfield light microscopy to determine their position on the grid and tile scans were generated. The samples were then processed using a Pelco BioWave Pro+ microwave (Ted Pella Inc, Redding, USA) and following a protocol adapted from the National Centre for Microscopy and Imaging Research protocol ⁴⁸. See Supplementary Table 17 for full BioWave program details. Each step was performed in the Biowave, except for the PB and water wash steps, which consisted of two washes on the bench followed by two washes in the Biowave without vacuum (at 250 W for 40 seconds). All the chemical incubations were performed in the Biowave for 14 minutes under vacuum in 2-minutes cycles alternating with/without 100W power. The SteadyTemp plate was set to 21°C unless otherwise stated. In brief, the samples were fixed again in 2.5% (v/v) glutaraldehyde (TAAB) / 4% (v/v) formaldehyde in 0.1M PB. The cells were then stained with 2% (v/v) osmium tetroxide (TAAB) / 1.5% (v/v) potassium ferricyanide (Sigma), incubated in 1% (w/v) thiocarbohydrazide (Sigma) with SteadyTemp plate set to 40°C, and further stained with 2% osmium tetroxide in ddH₂O (w/v). The cells were then incubated in 1% aqueous uranyl acetate (Agar Scientific, Stansted, UK) with SteadyTemp plate set to 40°C, and then washed in dH₂O with SteadyTemp set to 40°C. Samples were then stained with Walton's lead aspartate with SteadyTemp set to 50°C, and dehydrated in a graded ethanol series (70%, 90%, and 100%, twice each), at 250 W for 40 seconds without vacuum. Exchange into Durcupan ACM® resin (Sigma) was performed in 50% resin in ethanol, followed by 4 pure Durcupan steps, at 250 W for 3 minutes, with vacuum cycling (on/off at 30-seconds intervals), before embedding at 60°C for 48 hours. Blocks were trimmed to a small trapezoid, excised from the resin block, and attached to a serial block-face scanning electron microscopy (SBF SEM) specimen holder using conductive epoxy resin.

Prior to commencement of a SBF SEM imaging run, the sample were coated with a 2 nm layer of platinum to further enhance conductivity. SBF SEM data was collected using a 3View2XP (Gatan, Pleasanton, CA) attached to a Sigma VP SEM (Carl Zeiss Ltd, Cambridge, UK). Inverted backscattered electron images were acquired through the entire extent of the region of interest. For each of the 50-nm slices needed to image the cells in their whole volume, a low-resolution overview image (horizontal frame width 103 μm ; pixel size of 40 nm; using a 2 $\mu\text{seconds}$ dwell time) and a high-resolution image of the cell of interest (horizontal frame width 32 and 39 μm respectively; pixel size of 8 nm; using a 2 $\mu\text{seconds}$ dwell time) were acquired. The SEM was operated in high vacuum with focal charge compensation on (70%). The 30 μm aperture was used, at an accelerating voltage of 1.8 kV. Only minor adjustments in image alignment were needed and were done using the TrakEM2 plug-in of the FIJI framework ⁴⁹.

Immunohistochemistry. Whole sections from subcutaneous tumours (A375P/A375M2, WM983A/WM983B) and two tissue microarrays including a total of 48 primary melanoma tumours and 43 metastases, were used. Patient biopsies were obtained with approvals from the Ethics and Scientific Committee and specific informed patient consent ³¹. The IFs were delimited as the tumour areas showing at least 50% contact with the matrix, as previously described ^{5-7, 31}. All samples were formalin-fixed paraffin-embedded tissue. Samples were sectioned (3-4 μm thick) and dried for one hour at 65°C. Next, samples were deparaffined and rehydrated and endogenous peroxidase activity was blocked with 3% H_2O_2 in ethanol absolute for 10 minutes. Heat-induced epitope retrieval was carried out using 1:100 pH 6 Citrate Buffer H-3300 for 10 minutes at 100°C in a Biocare Decloaking Chamber (DC2012). Incubation with primary antibody in Zytomed antibody diluent was carried out for 40 minutes. Incubation with secondary antibody polymer conjugated (ImmPRESS Polymer Reagent) was carried out for 45 minutes. Incubation with Vector VIP HRP substrate chromogen was done for up to 10 minutes. All reagents used for detection were from VECTASTAIN ABC-HRP Kit (PK-4000). All samples were counterstained with hematoxylin. Lastly, samples were dehydrated, and slides were mounted. Reagents were used at RT in humidified slide chambers. Primary antibodies were: LAP1 (1:100; #21459-1-AP) from Proteintech; melanA (1:100, #ab51061). Whole section images were obtained from each sample using a NanoZoomer S210 slide scanner (Hamamatsu, Japan). Image analysis was done using QuPath software ⁵⁰. Positive cell detection was carried out and threshold to the intensity scores (0, 1, 2, 3) were applied. Then, QuPath software was trained to differentiate tumour cells from stroma, staining was graded semiquantitatively and H-scores were calculated as previously described ³¹. Co-localisation analysis was conducted for LAP1 and melanA staining as previously described ³¹.

Gene enrichment analysis. Normalised gene expression microarray data was obtained from GSE23764 ⁶. A375M2 were compared to A375P and to A375M2 treated with contractility inhibitors (H1152, Y27632 or blebbistatin). A catalogue of nuclear gene sets was downloaded, and analyses were carried out using GSEA software (<http://www.broadinstitute.org/gsea/index.jsp>). Permutations were set to 1000, permutation type to gene-set and t-test was established for ranking. GO gene sets were classified according to GO ontologies. Upregulated gene sets were filtered based on $\text{FDR} < 5\%$ and $\text{p-value} < 0.05$.

Gene expression analyses. Gene expression data from cells was obtained from publicly available datasets and normalised as previously described^{34, 51}. Data from 28 melanocytes was obtained from four melanocyte datasets from³⁴ (GSE4570, GSE4840),⁵² and⁵³, and data from melanoma cell lines (Philadelphia cohort GSE4841 (29 samples) and Mannheim cohort GSE4843 (37 samples)) where obtained from³⁴. Heatmaps for gene expression in cells were generated using MeV_4_9_0 software (<http://mev.tm4.org/>). Gene expression data from human samples was derived from three publicly available datasets from³⁶ (Riker GSE755333 (14 primary and 40 metastatic melanomas)),³⁵ (Kabbarah GSE4651732 (31 primary and 73 metastatic melanomas)) and³⁷ (Xu GSE840134 (31 primary and 52 metastatic melanomas)).

Statistical analyses. Unpaired t test, one-way ANOVA and two-way ANOVA with Tukey's post hoc tests were performed using GraphPad Prism (GraphPad Software, Inc). All results were obtained from at least three independent experiments unless otherwise stated. Data is plotted as minimum to maximum boxplots or graphs with the mean \pm standard error of the mean (SEM). The threshold for statistical was set to a p-value of less than 0.05.

REFERENCES

1. Oppenheimer, S.B. Cellular basis of cancer metastasis: A review of fundamentals and new advances. *Acta Histochem* **108**, 327-334 (2006).
2. Hanahan, D. & Weinberg, R.A. Hallmarks of cancer: the next generation. *Cell* **144**, 646-674 (2011).
3. Zbytek, B. *et al.* Current concepts of metastasis in melanoma. *Expert Rev Dermatol* **3**, 569-585 (2008).
4. Apalla, Z., Lallas, A., Sotiriou, E., Lazaridou, E. & Ioannides, D. Epidemiological trends in skin cancer. *Dermatol Pract Concept* **7**, 1-6 (2017).
5. Orgaz, J.L. *et al.* Diverse matrix metalloproteinase functions regulate cancer amoeboid migration. *Nat Commun* **5**, 4255 (2014).
6. Sanz-Moreno, V. *et al.* ROCK and JAK1 signaling cooperate to control actomyosin contractility in tumor cells and stroma. *Cancer Cell* **20**, 229-245 (2011).
7. Cantelli, G. *et al.* TGF-beta-Induced Transcription Sustains Amoeboid Melanoma Migration and Dissemination. *Current biology : CB* **25**, 2899-2914 (2015).
8. Orgaz, J.L. *et al.* Myosin II Reactivation and Cytoskeletal Remodeling as a Hallmark and a Vulnerability in Melanoma Therapy Resistance. *Cancer Cell* **37**, 85-103 e109 (2020).
9. Georgouli, M. *et al.* Regional Activation of Myosin II in Cancer Cells Drives Tumor Progression via a Secretory Cross-Talk with the Immune Microenvironment. *Cell* **176**, 757-774 e723 (2019).
10. Haeger, A., Krause, M., Wolf, K. & Friedl, P. Cell jamming: collective invasion of mesenchymal tumor cells imposed by tissue confinement. *Biochim Biophys Acta* **1840**, 2386-2395 (2014).
11. Liu, Y.J. *et al.* Confinement and low adhesion induce fast amoeboid migration of slow mesenchymal cells. *Cell* **160**, 659-672 (2015).

12. Weigelin, B., Bakker, G.J. & Friedl, P. Intravital third harmonic generation microscopy of collective melanoma cell invasion: Principles of interface guidance and microvesicle dynamics. *Intravital* **1**, 32-43 (2012).
13. Wolf, K. *et al.* Physical limits of cell migration: control by ECM space and nuclear deformation and tuning by proteolysis and traction force. *J Cell Biol* **201**, 1069-1084 (2013).
14. Khatau, S.B. *et al.* The distinct roles of the nucleus and nucleus-cytoskeleton connections in three-dimensional cell migration. *Sci Rep* **2**, 488 (2012).
15. Kirby, T.J. & Lammerding, J. Emerging views of the nucleus as a cellular mechanosensor. *Nat Cell Biol* **20**, 373-381 (2018).
16. Harada, T. *et al.* Nuclear lamin stiffness is a barrier to 3D migration, but softness can limit survival. *J Cell Biol* **204**, 669-682 (2014).
17. Dechat, T. *et al.* Nuclear lamins: major factors in the structural organization and function of the nucleus and chromatin. *Genes Dev* **22**, 832-853 (2008).
18. Cho, S., Irianto, J. & Discher, D.E. Mechanosensing by the nucleus: From pathways to scaling relationships. *J Cell Biol* **216**, 305-315 (2017).
19. Schirmer, E., Meinke, P., Makarov, A., Lê Thành, P. & Sadurska, D. Nucleoskeleton dynamics and functions in health and disease. *Cell Health and Cytoskeleton* (2015).
20. Haque, F. *et al.* SUN1 interacts with nuclear lamin A and cytoplasmic nesprins to provide a physical connection between the nuclear lamina and the cytoskeleton. *Mol Cell Biol* **26**, 3738-3751 (2006).
21. De Vos, W.H. *et al.* Repetitive disruptions of the nuclear envelope invoke temporary loss of cellular compartmentalization in laminopathies. *Hum Mol Genet* **20**, 4175-4186 (2011).
22. Le Berre, M., Aubertin, J. & Piel, M. Fine control of nuclear confinement identifies a threshold deformation leading to lamina rupture and induction of specific genes. *Integr Biol (Camb)* **4**, 1406-1414 (2012).
23. Vargas, J.D. Transient nuclear envelope rupturing during interphase in human cancer cells. *Nucleus* **3**, 88-100 (2012).
24. Raab, M. *et al.* ESCRT III repairs nuclear envelope ruptures during cell migration to limit DNA damage and cell death. *Science* **352**, 359-362 (2016).
25. Irianto, J. *et al.* DNA Damage Follows Repair Factor Depletion and Portends Genome Variation in Cancer Cells after Pore Migration. *Current biology : CB* **27**, 210-223 (2017).
26. Denais Nuclear envelope rupture and repairs during cancer cell migration. *Science* **352**, 353-358 (2016).
27. Lomakin, A.J. *et al.* The nucleus acts as a ruler tailoring cell responses to spatial constraints. *Science* **370** (2020).
28. Pandya, P., Orgaz, J.L. & Sanz-Moreno, V. Modes of invasion during tumour dissemination. *Mol Oncol* **11**, 5-27 (2017).
29. Tolde, O. *et al.* Quantitative phase imaging unravels new insight into dynamics of mesenchymal and amoeboid cancer cell invasion. *Sci Rep* **8**, 12020 (2018).
30. Ruprecht, V. *et al.* Cortical contractility triggers a stochastic switch to fast amoeboid cell motility. *Cell* **160**, 673-685 (2015).
31. Rodriguez-Hernandez, I. *et al.* WNT11-FZD7-DAAM1 signalling supports tumour initiating abilities and melanoma amoeboid invasion. *Nat Commun* **11**, 5315 (2020).

32. Clark, E.A., Golub, T.R., Lander, E.S. & Hynes, R.O. Genomic analysis of metastasis reveals an essential role for RhoC. *Nature* **406** (2000).
33. Subramanian, A. *et al.* Gene set enrichment analysis: a knowledge-based approach for interpreting genome-wide expression profiles. *Proc Natl Acad Sci U S A* **102**, 15545-15550 (2005).
34. Hoek, K.S. *et al.* Metastatic potential of melanomas defined by specific gene expression profiles with no BRAF signature. *Pigment Cell Res* **19**, 290-302 (2006).
35. Kabbarah, O. *et al.* Integrative genome comparison of primary and metastatic melanomas. *PLoS One* **5**, e10770 (2010).
36. Riker, A.I. *et al.* The gene expression profiles of primary and metastatic melanoma yields a transition point of tumor progression and metastasis. *BMC Med Genomics* **1**, 13 (2008).
37. Xu, L. *et al.* Gene expression changes in an animal melanoma model correlate with aggressiveness of human melanoma metastases. *Mol Cancer Res* **6**, 760-769 (2008).
38. Santos, M. *et al.* Identification of a novel human LAP1 isoform that is regulated by protein phosphorylation. *PLoS One* **9**, e113732 (2014).
39. Foisner R., G.L. Integral membrane proteins of the nuclear envelope interact with lamins and chromosomes, and binding is modulated by mitotic phosphorylation *Cell* **73**, 1267-1279 (1993).
40. Luithle, N. *et al.* Torsin ATPases influence chromatin interaction of the Torsin regulator LAP1. *Elife* **9** (2020).
41. Gillingham, A.K., Bertram, J., Begum, F. & Munro, S. In vivo identification of GTPase interactors by mitochondrial relocalization and proximity biotinylation. *Elife* **8** (2019).
42. Paluch, E.K. & Raz, E. The role and regulation of blebs in cell migration. *Curr Opin Cell Biol* **25**, 582-590 (2013).
43. Srivastava, N. *et al.* Nuclear fragility, blaming the blebs. *Curr Opin Cell Biol* **70**, 100-108 (2021).
44. Venturini, V. *et al.* The nucleus measures shape changes for cellular proprioception to control dynamic cell behavior. *Science* **370** (2020).
45. Rianna, C., Radmacher, M., Kumar, S. & Discher, D. Direct evidence that tumor cells soften when navigating confined spaces. *Molecular Biology of the Cell* **31**, 1726-1734 (2020).
46. Roberts, A.B. *et al.* Tumor cell nuclei soften during transendothelial migration. *J Biomech* **121**, 110400 (2021).
47. Rudzka, D.A. *et al.* Migration through physical constraints is enabled by MAPK-induced cell softening via actin cytoskeleton re-organization. *J Cell Sci* **132** (2019).
48. Deerinck, T., Bushong, E., Thor, A., Ellisman, M. & Thor, C. (2010).
49. Cardona, A. *et al.* TrakEM2 software for neural circuit reconstruction. *PLoS One* **7**, e38011 (2012).
50. Bankhead, P. *et al.* QuPath: Open source software for digital pathology image analysis. *Sci Rep* **7**, 16878 (2017).
51. Orgaz, J.L. *et al.* 'Loss of pigment epithelium-derived factor enables migration, invasion and metastatic spread of human melanoma'. *Oncogene* **28**, 4147-4161 (2009).
52. Ryu, B., Kim, D.S., Deluca, A.M. & Alani, R.M. Comprehensive expression profiling of tumor cell lines identifies molecular signatures of melanoma progression. *PLoS One* **2**, e594 (2007).

53. Magnoni, C. *et al.* Transcriptional profiles in melanocytes from clinically unaffected skin distinguish the neoplastic growth pattern in patients with melanoma. *Br J Dermatol* **156**, 62-71 (2007).

FIGURE LEGENDS

Figure 1. Metastatic melanoma cells can better negotiate repetitive constrained migration challenges than primary melanoma cells

(a) Schematic of transwell assays. Briefly, cells were challenged to migrate through transwells once or collected after a first round of migration and challenged repeatedly. The arrows indicate the direction for chemotactic migration. **(b)** Nuclear translocation rates of primary melanoma WM983A and metastatic melanoma WM983B cells after one round of migration in transwells of various pore sizes. **(c)** Relative percentage of nuclei with nuclear envelope blebs in WM983A and WM983B cells that translocated in one round through transwells. $n = 1758$ and 1728 , respectively. **(d)** Representative pictures of WM983A and WM983B expressing GFP-NLS (green) and stained for DNA (blue) after a second round of transwell migration. Transwell pores could be visualised using transmitted light. The magnifications show nuclei that translocated and display nuclear envelope blebs. Nuclear envelope blebs are indicated by white arrow heads. Scale bars, $30\ \mu\text{m}$ and $10\ \mu\text{m}$ magnifications. **(e)** Nucleus translocation rates of WM983A and WM983B cells after a second round of transwell migration. **(f)** Relative percentage of nuclei with nuclear envelope blebs in WM983A and WM983B cells that translocated in two rounds through transwells. $n = 192$ and 313 , respectively. **(g)** Nuclear translocation rates of WM983A and WM983B cells after one round of transwell migration and ROCK inhibitor (ROCKi) GSK269962A treatment. **(h)** Relative percentage of WM983A and WM983B cells with nuclear envelope blebs that translocated in one round through transwells with ROCKi treatment. $n = 1689$ and 1757 , respectively. **(i)** Nuclear translocation rates of WM983A and WM983B cells after two rounds of transwell migration and ROCKi treatment. **(j)** Relative percentage of nuclei with nuclear envelope blebs of WM983A and WM983B cells that translocated in two rounds through transwells with ROCKi treatment. $n = 1119$ and 1487 . Experimental data have been pooled from three individual experiments. Graphs show means and error bars represent SEM. p values calculated by one-way ANOVA, two-way ANOVA, and unpaired t test; * $p < 0.05$, *** $p < 0.001$, **** $p < 0.0001$.

Figure 2. The nuclear envelope of metastatic melanoma cells is highly dynamic

(a) Percentage of cell nuclei with nuclear envelope blebs in primary melanoma WM983A and metastatic melanoma WM983B cells. **(b)** Representative pictures of WM983B nuclei with nuclear envelope blebs of different shapes stained for lamin A/C (red) and DNA (blue). Scale bars, 10 μm . **(c)** Percentage of nuclei with nuclear envelope blebs according to bleb number and bleb shape per nucleus in WM983A and WM983B cells. $n= 434$ and 561 , respectively. **(d)** Percentage of cell nuclei with nuclear envelope blebs containing lamin A/C, lamin B1 or lamin B2 in WM983A and WM983B cells. $n= 605$ and 510 , respectively. **(e)** Representative picture of a WM983B cell nucleus with a typical nuclear envelope bleb stained for lamin A/C (green), lamin B1 (red) and DNA (blue). Scale bars, 10 μm . **(f) CLEM of representative image sequences of WM983B nuclei with an intact nuclear envelope bleb (left) and ruptured nuclear envelope blebs (right) and representative SBF SEM images of the same nuclei.** The white arrow indicates the site of rupture of the nuclear membranes. Scale bars, 5 μm . **(g)** Percentage of intact and ruptured nuclear envelope blebs in WM983A and WM983B cells over the course of 15 hours. **(h)** Percentage of intact and ruptured nuclear envelope blebs in WM983A and WM983B after treatment with ROCK inhibitor (ROCKi) GSK269962A over the course of 15 hours. **(i)** Duration of nuclear envelope repair in WM983A and WM983B cells. **(j)** Nuclear envelope rupture-repair events per hour in WM983A and WM983B cells over the course of 15 hours. $n= 1013$ and 1008 , respectively. Experimental data have been pooled from three individual experiments. **a, c, d, g, h** Graphs show means and error bars represent SEM. **i, j** Horizontal lines show the median and whiskers show minimum and maximum range of values. p values calculated by one-way ANOVA, two-way ANOVA and unpaired t test; * $p < 0.05$, ** $p < 0.01$, *** $p < 0.001$, **** $p < 0.0001$.

Figure 3. Nuclear transcriptomics reveals TOR1AIP1 upregulation in metastasis

(a) Flow diagram of GSEA carried out comparing the nuclear transcriptomes of highly amoeboid and highly metastatic melanoma A375M2 cells with less amoeboid and less metastatic melanoma A375P cells from data of gene expression microarray analysis. **(b)** The upper graphs show the distribution of upregulated and downregulated nuclear gene sets in A375M2 cells (left) and A375P cells (right). The lower graph shows the 12 most enriched GO gene set categories in A375M2. **(c)**

Section of heatmap of the leading-edge analysis showing cluster of upregulated nuclear envelope genes in A375M2 cells. **(d)** Flow diagram of the GSEA carried out comparing A375M2 cells with A375M2 cells treated with contractility inhibitors (ROCK inhibitors H1152 or Y27632 or myosin inhibitor blebbistatin) (A375M2_inh). The graphs show the distribution of upregulated and downregulated nuclear gene sets in A375M2 cells (left) and A375M2_inh (right). **(e)** Upregulated nuclear envelope genes selected from leading-edge analysis with their log₂ fold change in expression and statistical significance in A375M2 compared to A375P cells and in A375M2 compared to A375M2_inh. Statistically significant upregulated genes are coloured in pink in the table. **(f)** Fold regulation of candidate genes expression validated by qPCR in A375M2 compared to A375P. **(g)** Fold regulation of *OSBPL8*, *TOR1AIP1* and *SUMO1* expression validated by qPCR in metastatic melanoma WM983B compared to primary melanoma WM983A cells. **(h)** Heatmaps displaying fold change in expression of candidate genes in melanoma cell lines compared to melanocytes from Philadelphia and Mannheim datasets. **(i)** *TOR1AIP1* expression in primary tumours and metastasis in Kabbarah (n= 31 and 73, respectively), Riker (n= 14 and 40, respectively) and Xu (n= 31 and 52, respectively) melanoma patient datasets. Experimental data have been pooled from three individual experiments. **f, g** Graphs show means and error bars represent SEM. **i** Horizontal lines show the median and whiskers show minimum and maximum range of values. p values calculated by unpaired t tests; *p < 0.05, **p < 0.01, ***p < 0.001, ****p < 0.0001.

Figure 4. LAP1 is overexpressed in melanoma metastasis

(a) Representative images of tumour bodies (TB) and invasive fronts (IF) of WM983A and WM983B mouse melanoma xenografts. Scale bars, 50 µm. The magnifications show representative cell nuclei. Scale bars, 10 µm. **(b)** H-score for LAP1 staining in TBs and IFs of WM983A and WM983B mouse xenografts. **(c)** Percentage of tumour cell nuclei according to LAP1 intensity score in TBs and IFs of WM983A and WM983B mouse xenografts. n= 8 and 4, respectively. **(d)** Representative images of TBs and IFs of A375P and A375M2 mouse melanoma xenografts. Scale bars, 50 µm. The magnifications show representative cell nuclei. Scale bars, 10 µm. **(e)** H-score for LAP1 staining in TBs and IFs of A375P and A375M2 mouse xenografts. **(f)** Percentage of tumour cell nuclei according to LAP1 intensity score in TBs and IFs of A375P and A375M2 mouse xenografts. n= 8 and 7,

respectively. **(g)** Representative images of TB and IF of a primary tumour and a metastasis in human melanoma patient cohort A. Scale bars, 50 μm . The magnifications show representative cell nuclei. Scale bars, 10 μm . **(h)** H-score for LAP1 staining in TBs and IFs of primary tumours and metastases in cohort A by unpaired (left) or paired (right) analysis. **(i)** Percentage of tumour cell nuclei according to LAP1 intensity score in TBs and IFs of primary tumours and metastases in cohort A. $n = 19$ primary tumours and 14 metastases. **(j)** Representative images of TB and IF of a primary tumour and a metastasis in human melanoma patient cohort B. Scale bars, 50 μm . The magnifications show representative cell nuclei. Scale bars, 10 μm . **(k)** H-score for LAP1 staining in TBs and IFs of primary tumours and metastases in cohort B by unpaired (left) or paired (right) analysis. **(l)** Percentage of tumour cell nuclei according to LAP1 intensity score in TBs and IFs of primary tumours and metastases in cohort B. $n = 29$ primary tumours and 29 metastases. **b, e, h, k** Horizontal lines show the median and whiskers show minimum and maximum range of values. p values calculated by one-way ANOVA, two-way ANOVA and paired t-test; * $p < 0.05$, ** $p < 0.01$, *** $p < 0.001$, **** $p < 0.0001$.

Figure 5. LAP1 is required for repeated constrained migration

(a) Schematic of *TOR1AIP1* human gene transcription and translation. The gene is comprised of 10 exons and encodes a long protein isoform (584 aminoacids), LAP1B, and a short protein isoform (462 aminoacids), LAP1C. There are two transcripts produced by alternative splicing and each gives rise to a LAP1B variant: a full-length variant, variant 1, and a variant missing one alanine at position 185, variant 2. Note that here only one transcript has been represented for ease of presentation. LAP1C results from an alternative translation initiation site at position 122. The transmembrane domain has been coloured in light blue. Proteins have been drawn at aminoacid scale. **(b)** Representative immunoblot for LAP1 expression levels in melanocytes, primary melanoma cells and metastatic melanoma cells. **(c)** Quantification of LAP1B and LAP1C protein expression in panel of cell lines in (b). **(d)** Representative immunoblot for LAP1 expression levels in WM983B upon LAP1 siRNA transfection. **(e)** Nuclear translocation rates of control WM983B and WM983B with reduced LAP1 expression after a second round of transwell migration. **(f)** Relative percentage of nuclei with nuclear envelope blebs in control WM983B and WM983B with reduced LAP1 expression that translocated in two rounds through

transwells. $n = 872$ and 705 , respectively. **(g)** Invasion index of control WM983B and WM983B with reduced LAP1 expression in 3D collagen I matrices. **(h)** Representative images of control WM983B and WM983B with reduced LAP1 expression stained for DNA at $0 \mu\text{m}$ and up to $50 \mu\text{m}$ into collagen. Scale bars, $30 \mu\text{m}$. $n = 673$ and 539 , respectively. Experimental data have been pooled from three individual experiments. Graphs show means and error bars represent SEM. p values calculated by one-way ANOVA and unpaired t test; $**p < 0.01$, $***p < 0.001$.

Figure 6. LAP1B and LAP1C differentially regulate nuclear mechanics

(a) Schematic of mitochondrial retargeting assay. CAL51 cells were co-transfected with GFP-lamin A/C or GFP-lamin B1 and LAP1B^{NT}/LAP1B^{uNT}/LAP1C^{NT} tagged with HA-MTS. Where LAP1-lamin interaction occurs, GFP-lamin A/C or GFP-lamin B1 would be dragged from the nuclear envelope to the mitochondria or LAP1B^{NT}/LAP1B^{uNT}/LAP1C^{NT} tagged with HA-MTS would be dragged from the mitochondria to the nuclear envelope. **(b)** Representative images of experimental results for retargeting assay in CAL51 cells expressing GFP-lamin A/C or GFP-lamin B1 and stained for HA (red) and DNA (blue). Scale bars, $5 \mu\text{m}$. **(c)** Percentage of CAL51 cells showing co-localisation of GFP-lamin A/C (left) or GFP-lamin B1 (right) with LAP1B^{NT}/LAP1B^{uNT}/LAP1C^{NT}. Left graph, $n = 210$, 211 and 190 , respectively. Right graph, $n = 211$, 199 and 183 , respectively. Experimental data have been pooled from three individual experiments. Graphs show means and error bars represent SEM. p values calculated by one-way ANOVA; $*p < 0.05$, $**p < 0.01$, $***p < 0.001$, $****p < 0.0001$.

Figure 7. LAP1C supports a nucleus permissive for blebbing and constrained migration

(a) Nuclear translocation rates of primary melanoma WM983A cells, WM983A expressing LAP1C-mRuby3, LAP1B-mRuby3 or LAP1-mRuby3 and metastatic melanoma WM983B cells after a second round of transwell migration. **(b)** Relative percentage of nuclei with nuclear envelope blebs in WM983A cells, WM983A expressing LAP1C-mRuby3, LAP1B-mRuby3 or LAP1-mRuby3 and WM983B cells that translocated in two rounds through transwells. $n = 668$, 694 , 592 , 722 , 633 , respectively. **(c)** Schematic of LAP1B, LAP1B lacking lamin-binding region 1-72 (LAP1B ^{Δ 1-72}), LAP1B lacking its chromatin-binding region (LAP1B ^{Δ CBR}) and LAP1C.

Proteins have been drawn at aminoacid scale. **(d)** Nuclear translocation rates of WM983A expressing LAP1B-mRuby3 or LAP1B^{Δ1-72}-mRuby3 that translocated in two rounds through transwells. **(e)** Relative percentage of nuclei with nuclear envelope blebs in WM983A expressing LAP1B-mRuby3 or LAP1B^{Δ1-72}-mRuby3 after a second round of transwell migration. n= 629 and 678, respectively. **(f)** Nuclear translocation rates of WM983A expressing LAP1B-mRuby3 or LAP1B^{ΔC_{BR}}-mRuby3 that translocated in two rounds through transwells. **(g)** Relative percentage of nuclei with nuclear envelope blebs in WM983A expressing LAP1B-mRuby3 or LAP1B^{ΔC_{BR}}-mRuby3 after a second round of transwell migration. n= 518 and 545, respectively. **(h)** Nuclear translocation rates of WM983A expressing LAP1B-mRuby3 or LAP1B^{Δ1-72}-mRuby3, or resistant LAP1B-mRuby3 (LAP1B^R-mRuby3), LAP1B^{Δ1-72}-mRuby3 (LAP1B^{Δ1-72R}-mRuby3) or LAP1B^{ΔC_{BR}}-mRuby3 that translocated in two rounds through transwells upon treatment with LAP1 siRNA#1. **(i)** Relative percentage of nuclei with nuclear envelope blebs in WM983A expressing LAP1B-mRuby3, LAP1B^R-mRuby3, LAP1B^{Δ1-72}-mRuby3, LAP1B^{Δ1-72R}-mRuby3 or LAP1B^{ΔC_{BR}}-mRuby3 after a second round of transwell migration upon treatment with LAP1 siRNA#1. n= 322, 269, 305, 357, 368, 363, 400, 369, 372 and 375, respectively. Experimental data have been pooled from three individual experiments. **a, b, d, e, f, g, h, i** Graphs show means and error bars represent SEM. p values calculated by one-way ANOVA and unpaired t-test; *p<0.05, **p< 0.01, ***p< 0.001, ****p < 0.0001.

SUPPLEMENTARY FIGURE LEGENDS

Supplementary Figure 1. Multi-round transwell assays of melanoma cells

(a) Percentage of primary melanoma WM983A and metastatic melanoma WM983B cells that did not translocate after one round of migration in transwells of various pore sizes. **(b)** Relative percentage of WM983A and WM983B cells with nuclear envelope blebs that did not translocate in one round through transwells of various pore sizes. **(c)** Percentage of WM983A and WM983B translocated nuclei with nuclear envelope blebs according to bleb number and bleb shape after one round of migration in transwells of various pore sizes. n= 1758 and 1728, respectively. **(d)** Percentage of WM983A and WM983B cells that did not translocate on a second round of transwell migration. **(e)** Relative percentage of WM983A and WM983B cells

with nuclear envelope blebs that did not translocate on a second round of transwell migration. **(f)** Percentage of WM983A and WM983B translocated nuclei with nuclear envelope blebs according to bleb number and bleb shape after two rounds of migration in transwells. n= 192 and 313, respectively. **(g)** Nuclear translocation rates of WM983A and WM983B cells after three rounds of transwell migration. **(h)** Percentage of WM983A and WM983B cells that did not translocate on a third round of transwell migration. **(i)** Relative percentage of WM983A and WM983B cells with nuclear envelope blebs that translocated in three rounds through transwells. **(j)** Relative percentage of WM983A and WM983B cells with nuclear envelope blebs that did not translocate on a third round of transwell migration. n= 145 and 170, respectively. N=1. Experimental data have been pooled from three individual experiments unless otherwise stated. Graphs show means and error bars represent SEM. p values calculated by one-way ANOVA, two-way ANOVA and unpaired t test; *p < 0.05.

Supplementary Figure 2. Cell viability and actomyosin contractility in multi-round transwell assays

(a) Percentage of alive primary melanoma WM983A and metastatic melanoma WM983B cells after one round of transwell migration. **(b)** Percentage of alive WM983A and WM983B cells after two rounds of migration in transwells and staurosporin treatment. n= 180 and 213, respectively. N=1. **(c)** Representative pictures for (b) of WM983A and WM983B cells expressing GFP-NLS (green) and stained for caspase-3 (red) and DNA (blue). Scale bars, 30 μ m. **(d)** Representative immunoblot for primary melanoma WM983A and metastatic melanoma WM983B cells after treatment with ROCK inhibitor (ROCKi) GSK269962A. **(e)** Representative pictures of WM983A and WM983B cells treated with ROCKi and stained for pMLC2 (red), lamin A/C (green) and DNA (blue) before one round of transwell migration. Scale bars, 30 μ m. Experimental data have been pooled from three individual experiments unless otherwise stated. Graphs show means and error bars represent SEM. p values calculated by unpaired t test. n.s.: not significant.

Supplementary Figure 3. Nuclear shape changes in melanoma progression

(a) Percentage of nuclei with nuclear envelope blebs in M206 melanocytes. n= 120. N=1. **(b)** Representative pictures of M206 melanocytes stained for lamin A/C (red)

and DNA (blue). Scale bars, 30 μm . **(c)** Cell roundness index in primary melanoma WM983A and metastatic melanoma WM983B cells on collagen I. **(d)** Percentage of elongated and rounded cells in WM983A and WM983B on collagen I. **(e)** pMLC2 levels in WM983A and WM983B cells on collagen I. $n= 375$ and 425 , respectively. **(f)** Cell roundness index in less metastatic melanoma A375P and highly metastatic melanoma A375M2 cells on collagen I. **(g)** Percentage of elongated and rounded cells in A375P and A375M2 cells on collagen I. **(h)** pMLC2 levels in A375P and A375M2 cells on collagen I. $n= 385$ and 381 , respectively. **(i)** Representative images of WM983A, WM983B, A375P and A375M2 cells stained for pMLC2 (green), actin (red) and DNA (blue) on collagen I. Scale bars, 30 μm . The magnifications show representative cells. Scale bars, 10 μm . **(j)** Percentage of nuclei with nuclear envelope blebs in WM983A and WM983B cells on collagen I. **(k)** Nuclear circularity in WM983A and WM983B cells on collagen I. **(l)** Karyoplasmic ratio in WM983A and WM983B cells on collagen I. $n= 337$ and 373 , respectively. **(m)** Percentage of nuclei with nuclear envelope blebs in A375P and A375M2 cells on collagen I. **(n)** Nuclear circularity in A375P and A375M2 cells on collagen I. **(o)** Karyoplasmic ratio in A375P and A375M2 cells on collagen I. $n= 335$ and 331 , respectively. **(p)** Representative images of WM983A, WM983B, A375P and A375M2 cells stained for lamin A/C (green), actin (red) and DNA (blue) on collagen I. Scale bars 30 μm . The magnifications show representative cells. Scale bars, 10 μm . Experimental data have been pooled from three individual experiments. **a, d, g, j, m** Graphs show means and error bars represent SEM. **c, e, f, f, h, k, l, n, o** Horizontal lines show the median and whiskers show minimum and maximum range of values. p values calculated by two-way ANOVA, unpaired t test; ** $p < 0.01$, *** $p < 0.001$, **** $p < 0.0001$.

Supplementary Figure 4. Instability of nuclear envelope blebs in melanoma cells

(a) Percentage of nuclear envelope blebs positive for DNA damage markers (53BP1 and gamma-H2AX) in primary melanoma WM983A and metastatic melanoma WM983B cells. **(b)** Representative pictures of a WM983B nucleus with a nuclear envelope bleb positive for DNA damage stained for Gamma-H2AX (green), 53BP1 (red) and DNA (blue). Scale bars, 10 μm . **(c)** Relative Gamma-H2AX and 53BP1 fluorescence intensity levels and average Gamma-H2AX and 53BP1 foci per nucleus

in WM983A and WM983B cells with or without nuclear envelope blebs. n= 246 and 283, respectively. N=2. **(d)** Representative image sequence from repetitive, transient nuclear envelope rupture events in WM983A nucleus over 5 hours. **(e)** Representative image sequence from repetitive, transient nuclear envelope rupture events in a WM983B nucleus over 5 hours. Images showing the first frame of a nuclear envelope rupture in (d) or (e) are surrounded by a red square. Scale bars, 10 μm . Experimental data have been pooled from three individual experiments unless otherwise stated. Graphs show means and error bars represent SEM. p values calculated by two-way ANOVA, unpaired t test.

Supplementary Figure 5. LAP1 expression in tissue

(a) Karyoplasmic ratio of tumour cells according to LAP1 intensity score in tumor bodies (TB) and invasive fronts (IF) of WM983A and WM983B mouse xenografts. n= 8 and 4, respectively. **(b)** Karyoplasmic ratio of tumour cells according to LAP1 intensity score in TBs and IFs of A375P and A375M2 mouse xenografts. n= 8 and 8, respectively. **(c)** Representative pictures of normal skin stained for LAP1 (pseudocoloured in magenta), melanin (pseudocoloured in green) and DNA (pseudocoloured in blue). Scale bars, 50 μm and 30 μm , magnifications. **(d)** Levels of LAP1 measured in melanocytes and keratinocytes from pseudocoloured images. n= 20 and 20, respectively. **(e)** Karyoplasmic ratio of tumour cells according to LAP1 intensity score in TBs and IFs of primary tumours and metastases of human melanoma patient cohort A. n= 19 and 14, respectively. **(f)** Karyoplasmic ratio of tumour cells according to LAP1 intensity score in TBs and IFs of primary tumours and metastases of human melanoma patient cohort B. n= 29 and 29, respectively. **d** Horizontal lines show the median and whiskers show minimum and maximum range of values. p value calculated by unpaired t test; ****p < 0.0001.

Supplementary Figure 6. Impact of LAP1 siRNA on LAP1 expression, melanoma cell viability and migration

(a) Quantification of LAP1B and LAP1C expression in metastatic melanoma WM983B cells after 48 hours of LAP1 siRNA transfection with a siGENOME SMARTpool. **(b)** Percentage of alive WM983B control and WM983B with reduced LAP1 levels upon siGENOME SMARTpool transfection after one round of transwell migration. **(c)** Representative immunoblot for LAP1 expression levels in WM983B

cells after 48 hours of LAP1 siRNA transfection with ON-TARGETplus individual siRNAs. **(d)** Quantification of LAP1B and LAP1C expression in WM983B cells after 48 hours of LAP1 siRNA transfection with ON-TARGETplus individual siRNAs. **(e)** Nuclear translocation rates of control WM983B and WM983B with reduced LAP1 expression upon ON-TARGETplus individual siRNA transfection after a second round of transwell migration. Experimental data have been pooled from three individual experiments. Graphs show means and error bars represent SEM. p values calculated by one-way ANOVA and unpaired t test; n.s.: not significant, **p < 0.01, ***p < 0.001, ****p < 0.0001.

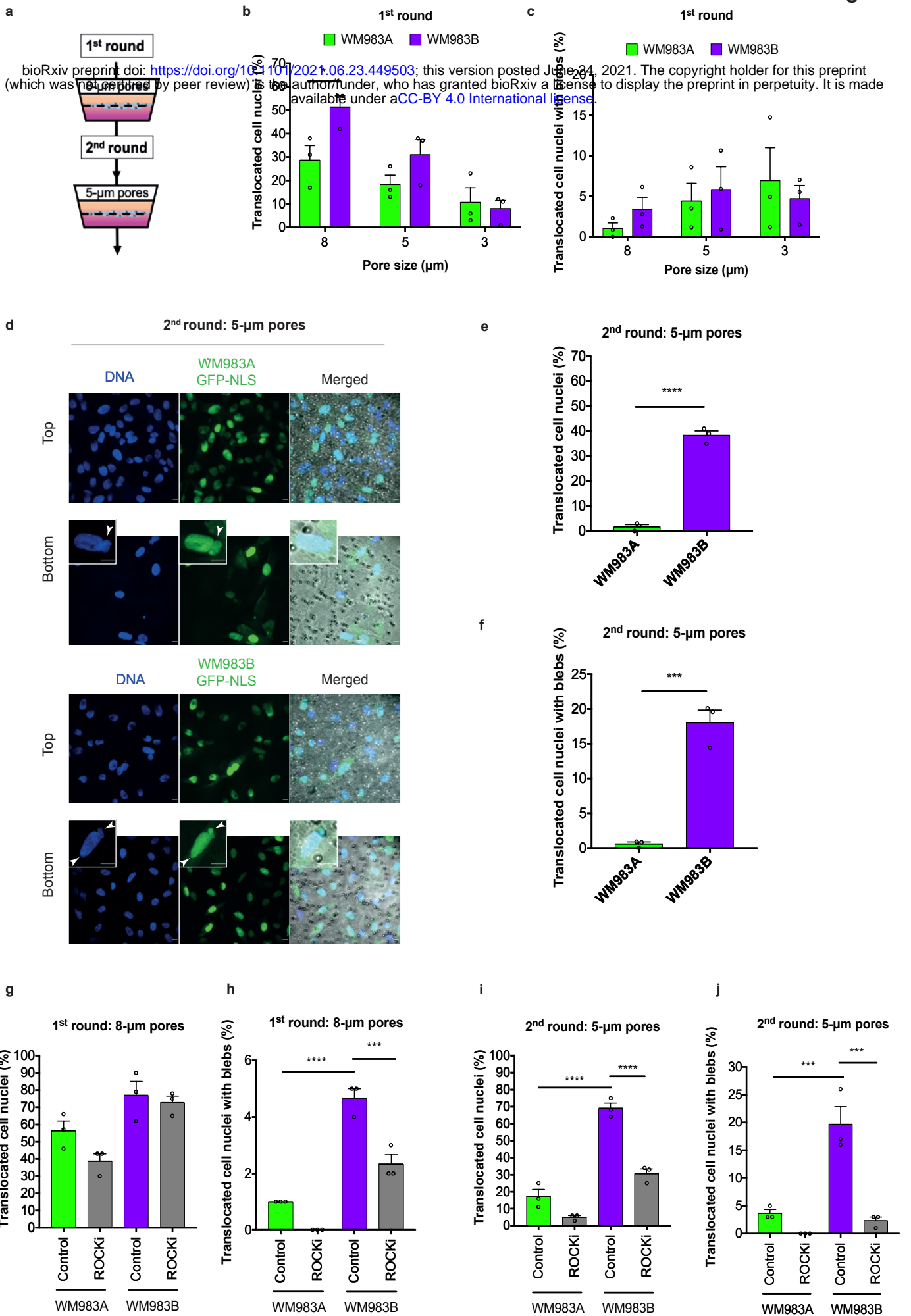
Supplementary Figure 7. Properties of LAP1 isoforms

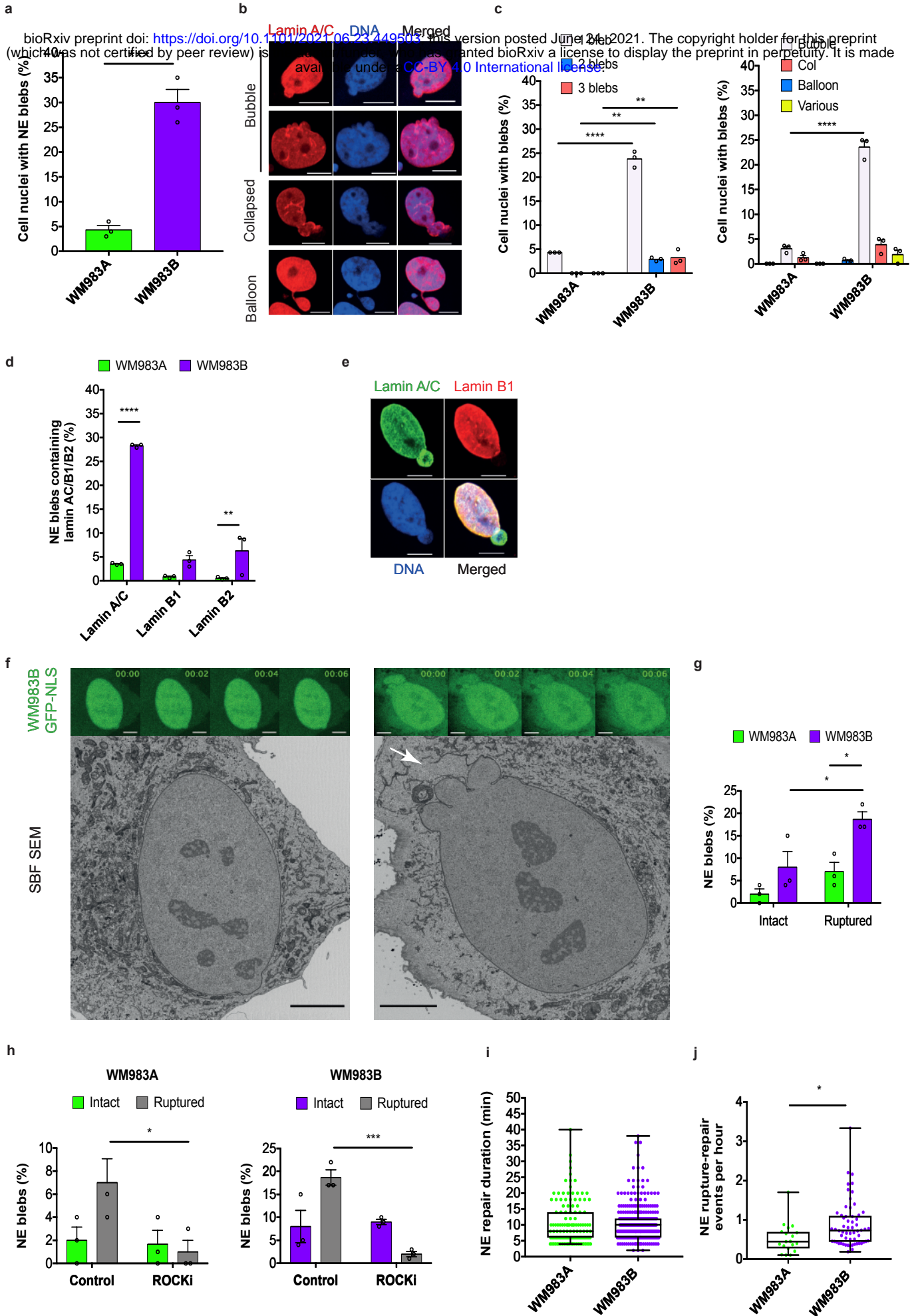
(a) LAP1 solubilisation assay in metastatic melanoma WM983B cells. S: supernatant; P: pellet. **(b)** Representative immunoblot for endogenous and exogenous LAP1 expression levels in primary melanoma WM983A cells, WM983A expressing LAP1C-mRuby3, LAP1B-mRuby3 (M122A) or LAP1-mRuby3 (allowing expression of both LAP1 isoforms) and metastatic melanoma WM983B cells. **(c)** Representative pictures of WM983B transfected with GFP-lamin A/C or GFP-lamin B1 and stably expressing LAP1B-mRuby3 or LAP1C-mRuby3 displaying nuclear envelope blebs. Scale bars, 5 μ m. **(d)** Levels of LAP1B-mRuby3, LAP1C-mRuby3, GFP-LAMIN A/C and GFP-LAMIN B1 measured in WM983B cells. n= 43, 63, 30 and 42, respectively. **(e)** Representative image sequence of FRAP experiment in WM983B cells co-expressing LAP1B-GFP and LAP1C-mRuby3. Scale bars, 5 μ m. The white arrowheads indicate where the cell was bleached at the main nuclear envelope and at the nuclear envelope bleb. **(f)** FRAP analysis of WM983B cells co-expressing LAP1B-GFP and LAP1C-mRuby3. n= 26. Experimental data have been pooled from three individual experiments. Graphs show means and error bars represent SEM. p values calculated by unpaired t tests; n.s.: not significant, *p < 0.05.

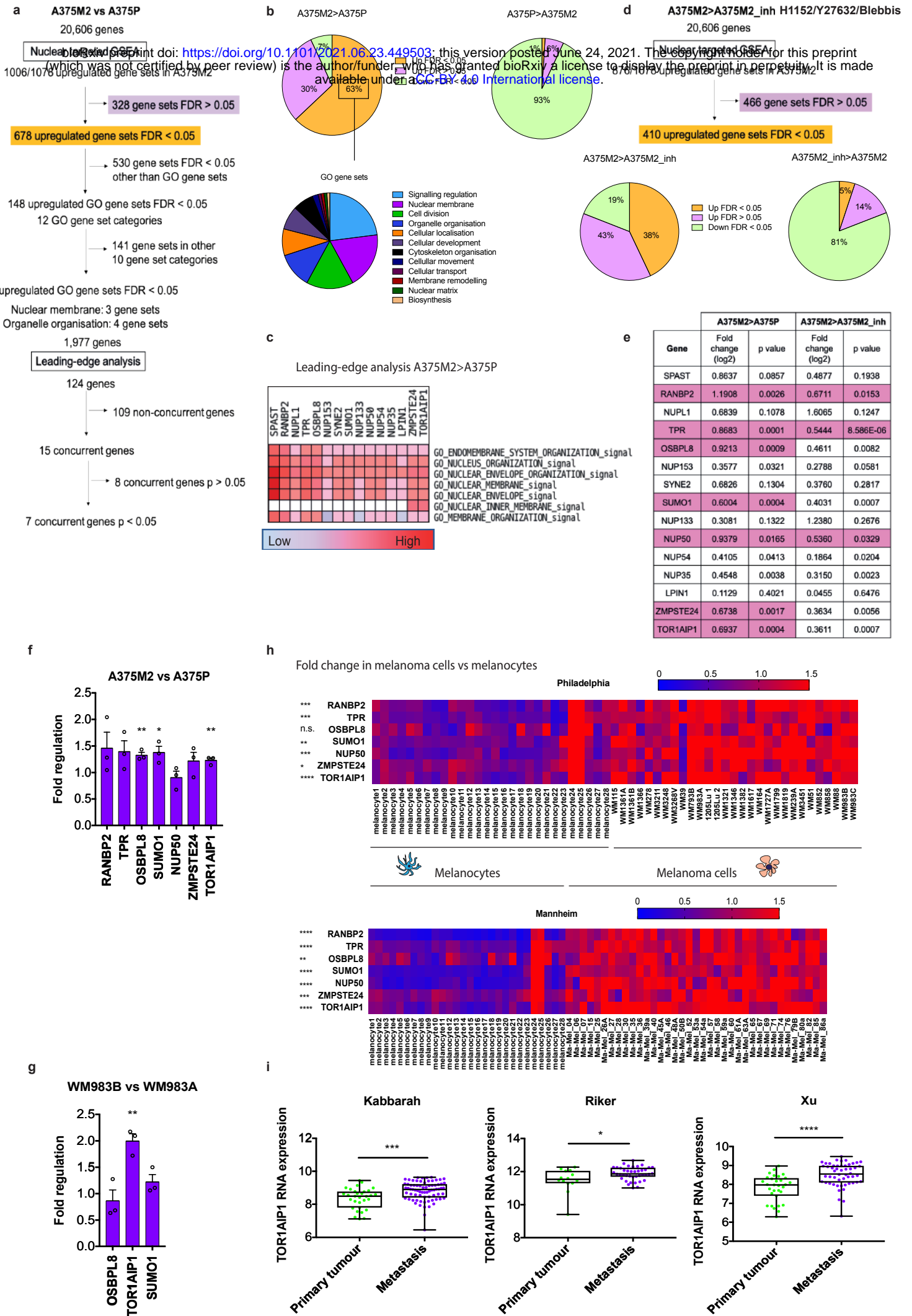
Supplementary Figure 8. LAP1C concentration-dependent effect on migration

(a) Fluorescence-activated cell sorting (FACS) dot plot of primary melanoma WM983A cells expressing GFP-NLS and LAP1C-mRuby3 according to levels of LAP1C-mRuby3 expression. **(b)** Representative immunoblot for endogenous and exogenous LAP1 expression levels in non-sorted WM983A cells and WM983A

sorted cells according to levels of LAP1C-mRuby3 expression. **(c)** Percentage of non-sorted WM983A cells and WM983A sorted cells according to LAP1C-mRuby3 expression that translocated after two rounds of migration in transwells. n= 664, 601, 462, 531, respectively. **(d)** Representative pictures of (c) of non-sorted WM983A cells and WM983A sorted cells according to LAP1C-mRuby3 expression expressing GFP-NLS (green) and stained for DNA (blue). Scale bars, 30 μ m. **(e)** Relative percentage of non-sorted WM983A cells and WM983A sorted cells according to LAP1C-mRuby3 expression with nuclear envelope blebs that translocated after two rounds of migration in transwells. Experimental data have been pooled from three individual experiments. Graphs show means and error bars represent SEM. p values calculated by one-way ANOVA; *p < 0.05.

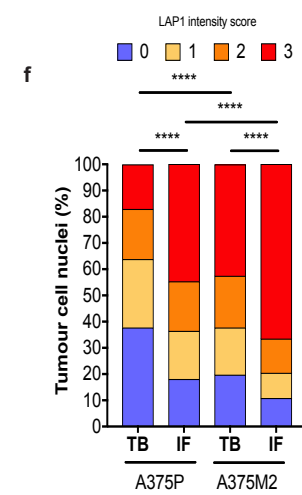
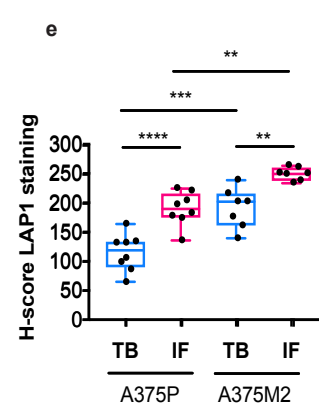
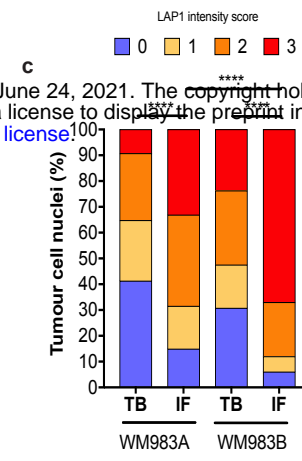
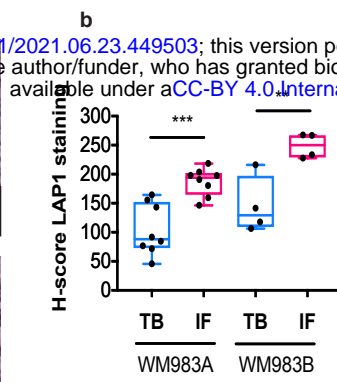
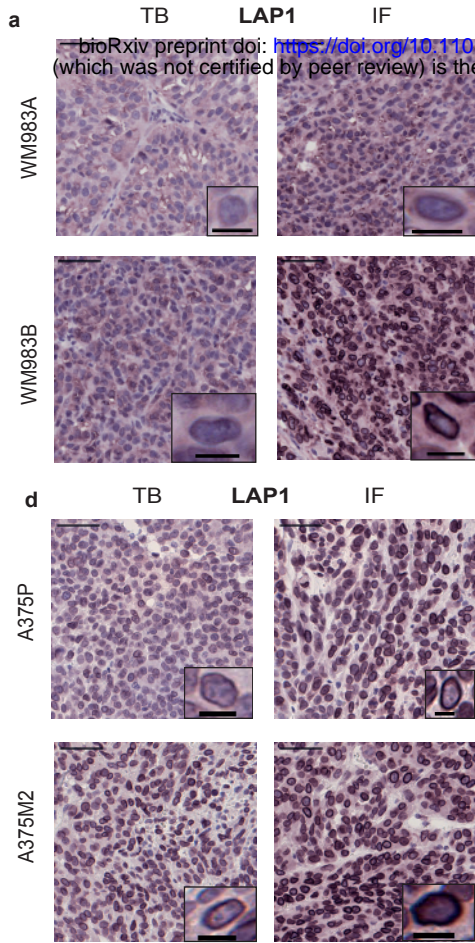




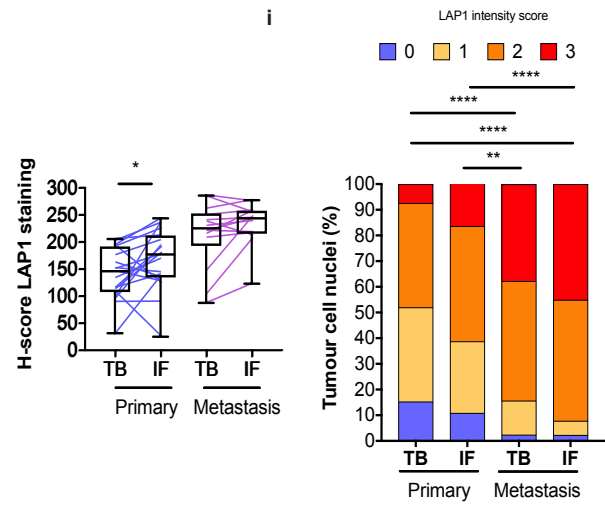
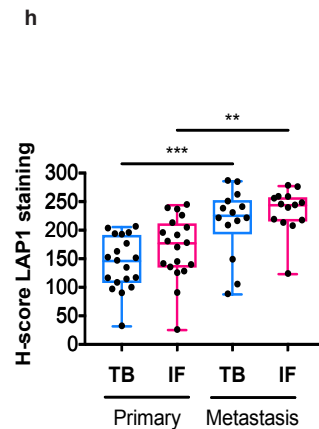
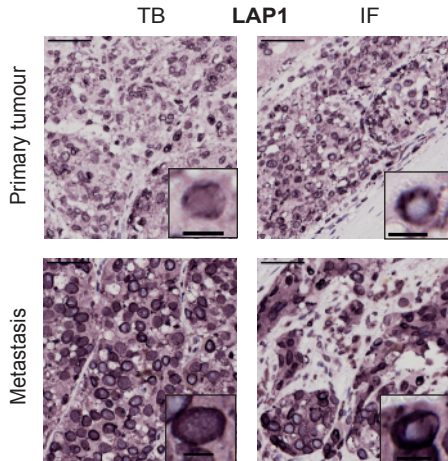




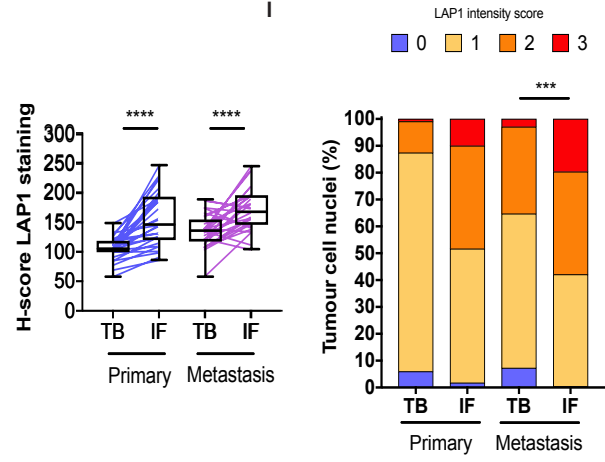
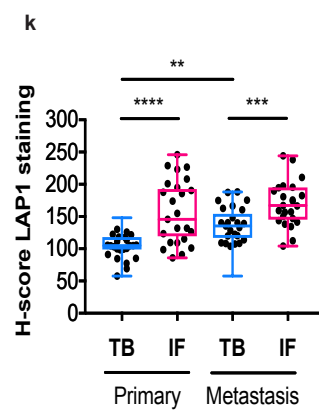
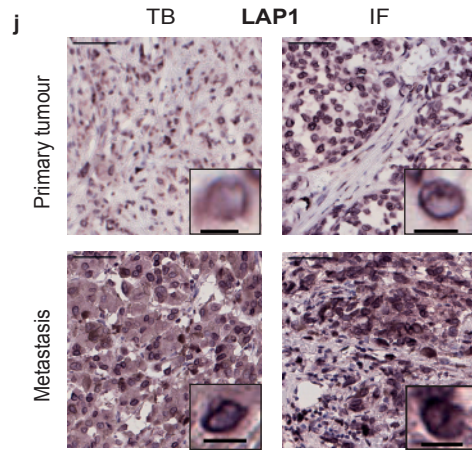
Mouse xenografts



Human melanoma patient cohort A



Human melanoma patient cohort B



bioRxiv preprint doi: <https://doi.org/10.1101/2021.06.23.449503>; this version posted June 24, 2021. The copyright holder for this preprint (which was not certified by peer review) is the author/funder, who has granted bioRxiv a license to display the preprint in perpetuity. It is made available under aCC-BY 4.0 International license.

